Performance Evaluation of the uEXPLORER Total-Body PET/CT Scanner Based on NEMA NU 2-2018 with Additional Tests to Characterize PET Scanners with a Long Axial Field of View

Benjamin A. Spencer*[1,2], Eric Berg*[1], Jeffrey P. Schmall[3], Negar Omidvari[1], Edwin K. Leung[1], Yasser G. Abdelhafez[2], Songsong Tang[4], Zilin Deng[4], Yun Dong[4], Yang Lv[4], Jun Bao[4], Weiping Liu[4], Hongdi Li[3], Terry Jones[2], Ramsey D. Badawi[1,2], and Simon R. Cherry[12]

[1]Department of Biomedical Engineering, University of California–Davis, Davis, California; [2]Department of Radiology, University of California–Davis, Davis, California; [3]United Imaging Healthcare, Houston, Texas; and [4]United Imaging Healthcare, Shanghai, China

The world's first total-body PET scanner with an axial field of view (AFOV) of 194 cm is now in clinical and research use at our institution. The uEXPLORER PET/CT system is the first commercially available total-body PET scanner. Here we present a detailed physical characterization of this scanner based on National Electrical Manufacturers Association (NEMA) NU 2-2018 along with a new set of measurements devised to appropriately characterize the total-body AFOV. **Methods:** Sensitivity, count-rate performance, time-of-flight resolution, spatial resolution, and image quality were evaluated following the NEMA NU 2-2018 protocol. Additional measurements of sensitivity and count-rate capabilities more representative of total-body imaging were performed using extended-geometry phantoms based on the world-average human height (~165 cm). Lastly, image quality throughout the long AFOV was assessed with the NEMA image quality (IQ) phantom imaged at 5 axial positions and over a range of expected total-body PET imaging conditions (low dose, delayed imaging, short scan duration). **Results:** Our performance evaluation demonstrated that the scanner provides a very high sensitivity of 174 kcps/MBq, a count-rate performance with a peak noise-equivalent count rate of approximately 2 Mcps for total-body imaging, and good spatial resolution capabilities for human imaging (≤3.0 mm in full width at half maximum near the center of the AFOV). Excellent image quality, excellent contrast recovery, and low noise properties were illustrated across the AFOV in both NEMA IQ phantom evaluations and human imaging examples. **Conclusion:** In addition to standard NEMA NU 2-2018 characterization, a new set of measurements based on extending NEMA NU 2-2018 phantoms and experiments was devised to characterize the physical performance of the first total-body PET system. The rationale for these extended measurements was evident from differences in sensitivity, count-rate–activity relationships, and noise-equivalent count-rate limits imposed by differences in dead time and randoms fraction between the NEMA NU 2 70-cm phantoms and the more representative total-body imaging phantoms. Overall, the uEXPLORER PET system provides ultra-high sensitivity that supports excellent spatial resolution and image quality throughout the field of view in both phantom and human imaging.

Key Words: PET; EXPLORER; total-body imaging; performance evaluation;

The University of California–Davis (UC Davis) and United Imaging Healthcare have collaborated to develop the world's first total-body PET scanner. The uEXPLORER PET/CT scanner has an axial field-of-view (AFOV) of 194.0 cm, allowing PET data collection from the entire human body simultaneously and greatly increasing PET scanner sensitivity.

Previous simulation studies have demonstrated the sensitivity gain that is expected to be provided with long-AFOV scanners (1–7). Work from Poon et al. (1,2) suggests that a 2-m-long lutetium oxyorthosilicate–based PET scanner would provide a sensitivity gain of approximately 40-fold for whole-body imaging, compared with a conventional PET scanner with an axial length of 21.8 cm.

The sensitivity gain offered by long-AFOV PET scanners opens up new possibilities for numerous research and clinical applications, including PET imaging with a much lower injected dose, late-time-point imaging, very fast imaging, and simultaneous total-body dynamic PET image acquisition (8,9). These potential breakthrough applications in clinical and research imaging (8,9) led to the creation of the EXPLORER consortium in 2011 (10). Through this consortium, UC Davis and United Imaging Healthcare collaborated to design, develop, and manufacture the world's first total-body PET scanner (uEXPLORER). Fabrication of the PET/CT scanner was completed in May 2018, and the uEXPLORER was granted 510(k) clearance from the U.S. Food and Drug Administration in December 2018. The uEXPLORER scanner was installed at the EXPLORER Molecular Imaging Center (UC Davis Health) in May 2019 (Fig. 1), with the first human imaging studies following in June 2019 and routine clinical use starting in August 2019. The EXPLORER consortium also supported development of the PennPET EXPLORER, a prototype PET scanner with a 64-cm AFOV (11,12)

FIGURE 1. Photograph of uEXPLORER total-body PET/CT scanner installed at EXPLORER Molecular Imaging Center in Sacramento, CA.

based on digital silicon photomultiplier detectors with direct crystal coupling. The performance evaluation of the PennPET EXPLORER reported state-of-the-art time-of-flight (TOF) resolution of 256 ps and high sensitivity (55 cps/kBq).

Previous studies have identified the advantages of longer-AFOV PET scanners (13,14), although all other state-of-the-art commercial scanners still range from 15 to 30 cm in AFOV (15–22). Watanabe et al. developed a 68.5-cm-long-AFOV prototype PET scanner as early as 2004 (13), with a sensitivity of 9.72 cps/kBq. Conti et al. also developed a 53-cm-long-AFOV PET scanner (14), which achieved a sensitivity of 19.87 cps/kBq; however, these scanners were never put into commercial production. Recently, a long-AFOV PET/CT prototype was developed by Siemens with an axial length of approximately 1 m (23). Additionally, cost-effective total-body imaging with plastic scintillators (J-PET) is in research development, with several constructed prototypes (24).

In preliminary human studies with the uEXPLORER, Badawi et al. demonstrated the capability of performing low-dose imaging (25 MBq of ^{18}F-FDG), late-time-point imaging (10 h after ^{18}F-FDG injection), fast imaging (<20 s static images), and simultaneous total-body dynamic imaging (25). Additionally, Zhang et al. reported total-body PET imaging with dynamic frames of just 100 ms to visualize cardiac motion (26). Here, we report a detailed physical characterization of the uEXPLORER PET/CT system using standard and newly designed phantom measurements to quantify important imaging metrics, including spatial resolution, count-rate performance, and quantitative image quality.

Characterization of PET scanners has commonly followed the National Electrical Manufacturers Association (NEMA) NU 2 standard (27), which defines a set of experiments and analyses using standardized imaging phantoms and permits valid comparisons between different PET systems. Although the NEMA NU 2-2018 measurements were performed in this characterization of the uEXPLORER scanner, these standards are defined only for PET scanners with an AFOV of no more than 65 cm and are not well suited for long-AFOV scanners, especially the 194-cm-long uEXPLORER, which is considerably longer than the 70-cm phantoms prescribed in the NEMA NU 2 tests. Therefore, a major component of this study was to devise a set of additional informative phantom measurements using extended phantom geometries and experiments that represent total-body imaging and provide a

representative performance evaluation of the uEXPLORER for total-body PET imaging. For these extended phantoms, lengths close to the world-average human height (165 cm (28)) were chosen. By making use of standard phantom components already in practice for the NEMA NU 2 tests that are commonly followed in the literature, the extended phantom measurements are intended to serve as a reasonable and applicable starting point in the standardized characterization of long-AFOV PET systems. All system and image evaluations were performed using in-house software developed at UC Davis.

MATERIALS AND METHODS

System Parameters

Physical Parameters of the Scanner. The uEXPLORER system comprises 8 PET units along the axial direction; each unit is 24.02 cm in axial length and 78.6 cm in diameter (detectors face-to-face), with a 0.26-cm gap between units, forming the system's total axial length of 194.0 cm. There are 24 detector modules in each PET unit, and each module contains 70 block-detectors arranged in a 5×14 matrix (transaxial $\times$ axial). The detector blocks comprise a 7×6 array of pixelated lutetium-yttrium oxyorthosilicate (LYSO) crystals, each $2.76 \times 2.76 \times 18.1$ mm, that are read out using four 6×6 mm silicon photomultipliers (SensL J-series). An integrated light-guide design is used to encode the crystal position among the 4 silicon photomultiplier signals, achieving an Anger multiplexing of 10.5:1. Detectors along the transaxial direction of the module share energy information so that Compton-scattered photons from edge crystals can be recovered; axial blocks are not in communication for Compton scatter recovery. The uEXPLORER system comprises 13,440 detector blocks with a total of 564,480 LYSO crystals and 53,760 silicon photomultiplier channels. The PET system is integrated with a 160-slice CT scanner, capable of helical acquisition (maximum rotation speed, 0.5 s) with a minimum slice thickness of 0.5 mm. A patient bed designed to accommodate total-body PET imaging provides precise alignment (<2-mm fusion accuracy) between PET and CT and with matched deflection.

Data Acquisition and Image Reconstruction. Each PET unit can form coincidence events with unit differences up to ± 4, for a maximum acceptance angle of 57.0°, and is fixed by the manufacturer and used for all tests in this study except the NEMA NU 2-2018 spatial resolution test. The total number of lines of response (LORs) collected are 92×10^9. A variable coincidence timing window is used for both prompt and delayed coincidence channels to accommodate the large range of possible LOR lengths with the large acceptance angle: for unit differences of 0, the coincidence timing window is 4.5 ns, whereas for the maximum unit difference of 4, a coincidence timing window of 6.9 ns is used. The TOF measurement is discretized in 39.06-ps bins. The scanner uses an energy window of 430–645 keV.

An 8-node computational cluster (vendor-provided) is used for data acquisition and image reconstruction. Raw coincidence data from each PET unit are transferred and stored locally on the computational cluster using a 10-Gbps network, allowing for event rates of up to 149 Mcps per PET unit. Before reconstruction, these data are merged to form a single time-ordered list-mode file. The cluster is used for the parallel list-mode TOF ordered-subset expectation maximization reconstruction framework with graphics processing unit acceleration. Image reconstruction with point-spread function (PSF) modeling in projection space is provided.

Our typical clinical image reconstruction protocol is performed with 4 TOF ordered-subset expectation maximization iterations, 20 subsets, a 2.344-mm isotropic voxel size, with and without PSF modeling. Unless otherwise stated, all images were reconstructed with

our clinical image reconstruction protocol with PSF modeling. Although often unavoidable in conventional PET, no image smoothing or filtering was applied to the reconstructed images in this study to best demonstrate the image quality and noise levels.

Data Corrections and Calibrations. A nonparalyzable response model was used for dead-time correction at the level of each detector block; this level of discretization was determined from previous studies (*29*) and accounts for the large count-rate differences encountered across the AFOV in a total-body scanner. Correction factors were obtained from a measurement using a uniform cylindric phantom (15 cm in diameter, 210 cm in length) with an initial activity of approximately 1,480 MBq (~40 mCi). The singles count-rates of each block are recorded in the list-mode file and are used to estimate the dead-time loss for each coincidence event, along with plane efficiency factors to account for oblique LORs (*29*). Normalization factors for detector efficiency and plane efficiency are also calculated using the data from the uniform cylindric phantom (*30*). Scatter is corrected using a Monte Carlo simulation–based method (*31*). A primary motivation of this method is to model multiple scatter events, which are more abundant in oblique LORs (*32*). Random coincidences are estimated using a delayed coincidence window implemented into the coincidence electronics hardware. The coregistered CT image is used for attenuation correction.

Sensitivity

System sensitivity was measured with 2 phantoms: a 70-cm line source (NEMA NU 2-2018) and a 170-cm line source, both filled with a low activity of ^{18}F (~4 MBq). The 70-cm line source measurement followed the NEMA NU 2-2018 protocol that uses a set of 5 concentric aluminum sleeves to estimate attenuation-free sensitivity, whereas the 170-cm line source measurement was obtained without aluminum sleeves, with the assumption that the 511-keV photon attenuation from the line source was negligible and that the emitted positrons had sufficient stopping power in the 2-mm tubing wall thickness. The 170-cm filled tube line source was fastened to a taut guideline parallel to the axis of the scanner, attached on one end to the patient bed and on the opposite end to an external support positioned outside the scanner bore. Minimal (<5 mm) deflection was observed along the line source length in reconstructed images. List-mode data from the system were binned into single-slice rebinned (SSRB) sinograms and used to estimate the total sensitivity and axial slice sensitivity for both phantom lengths. Similar to the NEMA NU 2-2018 analysis methodology for sensitivity, the 170-cm line source axial sensitivity profile was calculated by dividing the prompt minus delay count rate obtained from each SSRB sinogram slice by the total activity in the line source, and the total sensitivity was computed as the sum of all SSRB sinogram slices. The line source activity was normalized according to the actual extent of the line source filled with ^{18}F solution (169.7 cm) relative to the nominal 170-cm length.

Count-Rate Performance

The count-rate performance of the uEXPLORER was assessed using a 70-cm-long NEMA NU 2-2018 scatter phantom and a 175-cm-long scatter phantom that was built using 10 segments from 3 NEMA NU 2-2018 scatter phantoms (Data Spectrum). Both phantoms include a fillable line source that is threaded through the length of the phantom. Count rates for trues, scatters, and random coincidences were extracted from prompt- and delayed-coincidence SSRB sinograms using the methods outlined in NEMA NU 2-2018 for both phantom lengths. Noise-equivalent count rate (NECR) was computed assuming a low-variance randoms estimate, that is, with a randoms multiplier of 1. The ideal trues rate was estimated using a linear fit of the measured trues at low activity, where dead-time losses are assumed negligible, and the difference between the extrapolated ideal trues and measured trues was used to estimate dead-time losses at each measured activity.

Only the SSRB sinogram slices within the central 65 cm of the AFOV were used for the 70-cm-long phantom as specified in NEMA NU 2-2018, whereas similarly, the central 170-cm SSRB sinograms were used for the 175-cm-long phantom. Both line sources were filled with approximately 1,100 MBq of ^{18}F at the start of the experiments.

TOF Resolution

TOF resolution was calculated according to the NEMA NU 2-2018 protocol that measures TOF resolution from the list-mode data generated in the 70-cm scatter phantom count-rate experiment. Only prompt coincidences traversing within ±20 mm from the line source are included, and the list-mode TOF values after correction for the position of the line source relative to the midpoint of the LOR are binned into a TOF histogram and used to compute full-width-at-half-maximum coincidence timing resolution. Subtraction of scatter and random coincidences is performed as described in NEMA NU 2-2018 using the tails of the TOF histograms. The vendor-provided timing offset corrections were applied during the list-mode processing step.

TOF resolution for individual LORs was also computed using a subset of the LORs that contains a sufficiently large number of counts. To acquire enough counts, a 37-MBq ^{68}Ge line source was used in place of the ^{18}F line source in the NEMA NU 2-2018 scatter phantom, and list-mode data were acquired for approximately 12 h. The same TOF processing was used as described for the NEMA NU 2-2018 TOF measurement, except exclusions were applied during processing to select events from individual LORs.
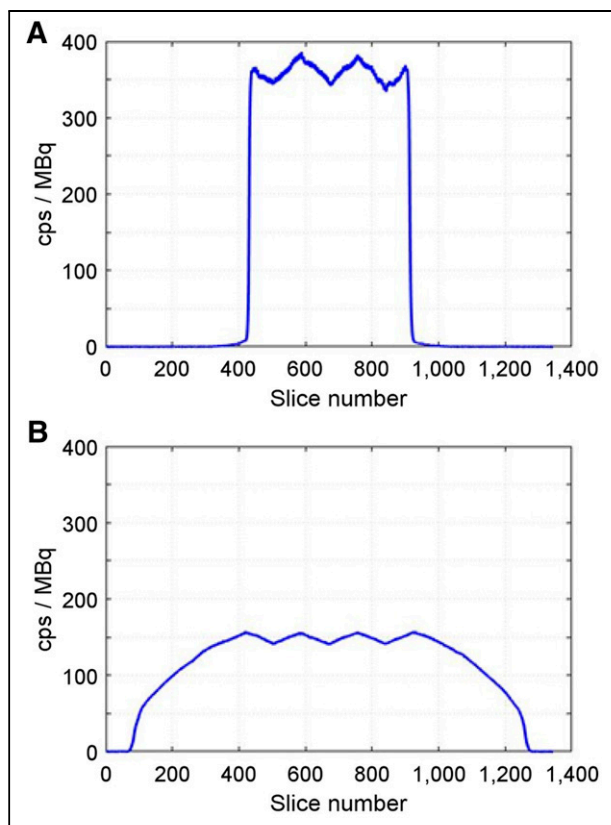

FIGURE 2. Axial sensitivity profiles for 70-cm (NEMA NU 2-2018) (A) and 170-cm (B) line source phantoms. Sinogram slice thickness is 1.444 mm.

Spatial Resolution

NEMA NU 2-2018 spatial resolution was measured by imaging ^{18}F ($\sim$300 kBq) capillary sources 0.5 mm in inner diameter with less than a 1-mm axial extent. To perform the analytic reconstruction as specified in the NEMA NU 2-2018 guidelines, the list-mode data were first Fourier-rebinned into 2-dimensional sinograms (33) and the sinograms were reconstructed into 1,023 × 1,023 image matrices (0.6 × 0.6 mm pixels) using 2-dimensional filtered backprojection (0.6-mm sinogram and image slice thickness). To minimize the Fourier rebinning error in the axial direction when using a large acceptance angle (34), the acceptance angle was restricted to the width of 1 unit (24 cm) for this measurement. The spatial resolution in full width at half maximum was computed following NEMA NU 2-2018. The presented data are an average of 2 separate measurements.

In addition, reconstructed spatial resolution with the 3-dimensional ordered-subset expectation maximization algorithm and using the standard acceptance angle (±4 units, 57°) was assessed using an ^{18}F-FDG ($\sim$20 MBq)–filled mini-Derenzo phantom (Data Spectrum). The diameter and edge-to-edge spacing of the activity-filled hollow channels were 1.2, 1.6, 2.4, 3.2, 4.0, and 4.8 mm. The phantom was imaged in 2 orientations (activity-filled rods in the transaxial plane and sagittal plane) and at 2 axial positions (axial center and center of the last PET unit; i.e., ¹⁄₁₆AFOV) to assess the effect of acceptance angle on reconstructed spatial resolution on both transaxial and axial resolution. Images were reconstructed with our high-resolution brain reconstruction parameters (1.172-mm isotropic voxels, 10 iterations) and without PSF to unambiguously demonstrate changes in spatial resolution.

Image Quality and Accuracy of Corrections

The NEMA IQ phantom was filled and imaged according to NEMA NU 2-2018. All spheres were filled with an ^{18}F-FDG solution at a sphere-to-background concentration ratio of 3.7:1 and with a background activity concentration of 5.1 kBq/mL. The IQ phantom was positioned with the spheres at the axial center of the PET field of view. A single bed position was used, with a scan duration of 30 min.

Images were reconstructed using the clinical image reconstruction protocol (2.344-mm isotropic voxels, 4 iterations, 20 subsets), both with and without PSF modeling, in addition to our high-resolution brain reconstruction protocol (1.172-mm isotropic voxels, 10 iterations, 20 subsets) with PSF modeling. The contrast recovery coefficient (CRC), background variability, and relative count error in the cold lung region were calculated using a semiautomated tool developed to define region-of-interest (ROI) boundaries and extract ROI statistics. In short, phantom center and sphere center coordinates were identified by parabolic fitting on regional image projections, and 2-dimensional circular ROI analysis was performed, taking the partial pixels into account.

The NEMA IQ phantom and methodology were also used to assess image quality with reduced scan durations or reduced ^{18}F activity. The impact of scan duration on image quality was measured by reconstructing the shorter time frames from the original 30-min-duration list-mode file to simulate shorter scan durations—as short as 30 s. The effect of the activity level on image quality was evaluated by scanning the NEMA IQ phantom at 18 time points, delayed by up to 12 h. The phantom was not moved between scans.

To evaluate the image quality throughout the AFOV, the NEMA IQ and scatter phantom were scanned at axial positions of ±39 cm and ±63 cm from the center of the AFOV; axial location was defined by the center of the image quality spheres. These positions were based on the axial sensitivity profile that corresponds to roughly 95% and 70% of the peak sensitivity. The scan durations ranged from 7.6 to 13.0 min from the first to the last acquisition to account for ^{18}F radioactivity decay. This phantom measurement had a sphere-to-background concentration ratio of 5.2:1 and a background activity concentration of 4.5 kBq/mL at the start of imaging.

Lastly, given that the CRC may be dependent on the sphere-to-background ratio, in addition to the previously described 2 sets of scans with sphere-to-background concentration ratios of 3.7:1 and 5.2:1 an additional NEMA IQ scan was performed at the center of the AFOV using a sphere-to-background concentration ratio of 9.0:1. The specifications of all NEMA IQ scans used for this comparison are summarized in Supplemental Table 1 (supplemental materials are available at http://jnm.snmjournals.org).

Human Imaging

Two studies from routine clinical care are presented to exemplify the uEXPLORER physical characterization results defined by phantom studies. The study data were collected through an institutional review board–approved retrospective study and a prospective study for which the subjects gave written informed consent. In the first study, a prostate cancer patient imaged for 10 min at 4 min after injection of 320 MBq (8.6 mCi) of ^{18}F-fluciclovine was used to demonstrate the spatial resolution characteristics in human imaging. In the second study, a lung cancer patient scanned
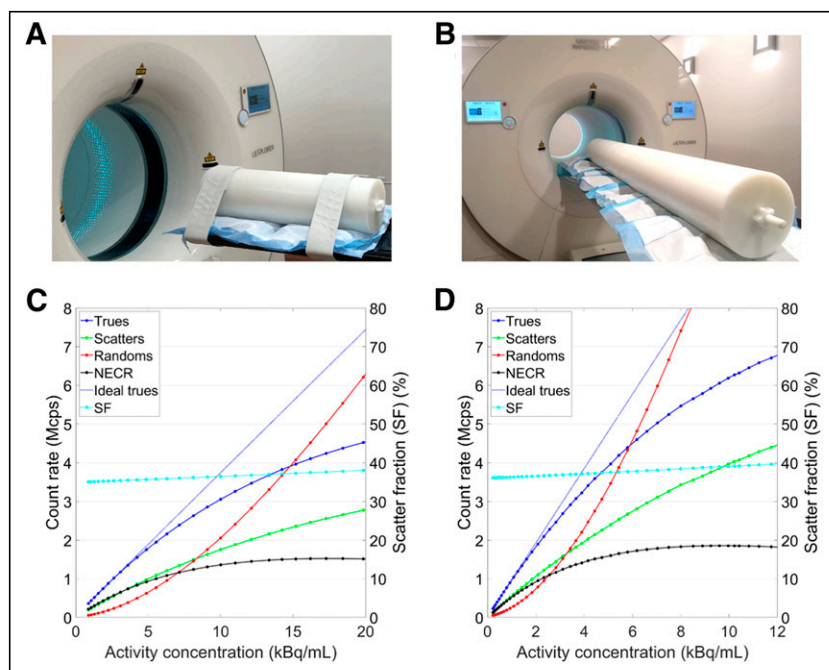

FIGURE 3. (A and B) 70-cm-long NEMA NU 2 scatter phantom (A) and 175-cm-long scatter phantom (B) assembled from multiple NEMA NU 2 phantoms on uEXPLORER PET/CT patient bed. (C and D) Measured count-rates with 70-cm-long (C) and 175-cm-long (D) scatter phantom. Count-rate measures are plotted vs. left vertical axes; scatter fractions are plotted vs. right vertical axes. Activity concentrations for A and B were computed by dividing total activity in phantom at each time-point by phantom volume (22 L for 70-cm-long phantom and 55 L for 175-cm-long phantom).

for 20 min after a 90-min uptake period of 188 MBq (5.09 mCi) of ^{18}F-FDG was used to illustrate the image quality and sensitivity of the scanner. Image reconstructions of shortened durations were also performed to depict count-dependent image quality. For both studies, the fractional dead time was estimated from the count-rate experiment using the 175-cm scatter phantom at the equivalent activity concentration.

RESULTS

Sensitivity

The NEMA NU 2-2018 sensitivity with the 70-cm-long line source filled with ^{18}F was 174 kcps/MBq at the center of the field of view and 177 kcps/MBq at a 10-cm radial offset. With the 170-cm-long line source, the total sensitivity was 147 kcps/MBq at the center and 151 kcps/MBq at a 10-cm radial offset. Axial sensitivity profiles (Fig. 2) showed a peak sensitivity plateau at ±48.5 cm from the center due to the maximum acceptance angle of ±4 ring units, with minor peaks and valleys within the plateau caused by the unit-difference–based coincidence selection, which leads to peak sensitivity at the midpoints of the 4 central PET units. This characteristic contrasts with conventional PET scanners, which use a maximum acceptance angle equal to that of the full axial extent of the system and therefore demonstrate triangular axial sensitivity profiles (15–22). The peak sensitivity estimated from the axial sensitivity profile for the 170-cm line source was approximately 18.6% (calculated by dividing the peak SSRB slice sensitivity [158 cps/MBq] by the fraction of activity contained in each slice [1 MBq/1,700 mm = 0.8 kBq/1.44 mm]). This sensitivity agrees closely with the NEMA NU 2-2018 sensitivity (174 kcps/MBq = 17.4%) and is expected given the plateau shape of the NEMA NU 2-2018 sensitivity profile (Fig. 2A).

Count-Rate Performance

Peak NECR with the 70-cm-long scatter phantom was 1,524 kcps at a 17.3 kBq/mL activity concentration, with a corresponding average scatter fraction of 36.3% (Fig. 3C). With the 175-cm-long scatter phantom, peak NECR increased to 1,855 kcps at 9.6 kBq/mL, with a corresponding average scatter fraction of 37.4% (Fig.

3D). At the peak NECR, the estimated dead-time losses in the trues rate were 34% with both the 70-cm and the 175-cm phantoms (Supplemental Fig. 1). Peak NECR with the 175-cm phantom agreed well with simulations of a 2-m-long PET scanner (validated against the Biograph mCT scanner [Siemens]) and demonstrated a 25- to 31-fold increase in NECR versus conventional PET systems (1,2).

TOF Resolution

TOF resolution measured with NEMA NU 2-2018 is shown versus activity concentration in Figure 4. Good TOF resolution stability was achieved, with less than 5% degradation from the lowest activity concentration up to the peak NECR activity concentration (17.3 kBq/mL). This minor decrease in TOF performance at higher activities may be related to pulse pile-up causing crystal misidentification or to other count-rate–dependent factors in the front-end electronics (e.g., baseline noise). There were no discernable differences in TOF resolution between the NEMA NU 2-2018 70-cm-long scatter phantom and the 175-cm-long scatter phantom as described. TOF resolution for individual LORs using the long-duration [68]Ge scan (equivalent activity concentration of ~2 kBq/mL) was 412 ± 35 ps. The average number of counts per LOR used to compute TOF resolution was about 2,000.

Spatial Resolution

Spatial resolution measured according to NEMA NU 2-2018 with an ^{18}F point source and Fourier-rebinned filtered backprojection reconstruction is summarized in Table 1. Reconstructed image slices of the mini-Derenzo phantom are provided in Figure 5. In the transaxial orientation (i.e., radial and tangential resolution components), there was a negligible difference in spatial resolution between the axial center (with a maximum acceptance angle of 57.0°) and the center of the last PET unit ($\frac{1}{16}$ AFOV, with a maximum acceptance angle of 17.0°). The 2.4-mm rods were clearly
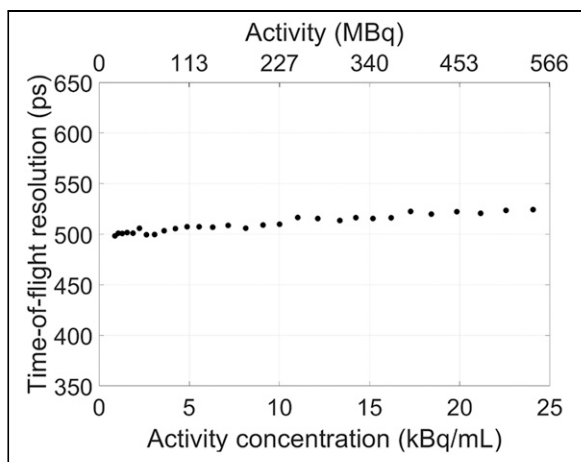

FIGURE 4. TOF resolution plotted vs. activity concentration using 70-cm-long NEMA NU 2 scatter phantom. TOF resolution of 505 ps at 5.3 kBq/mL was obtained.
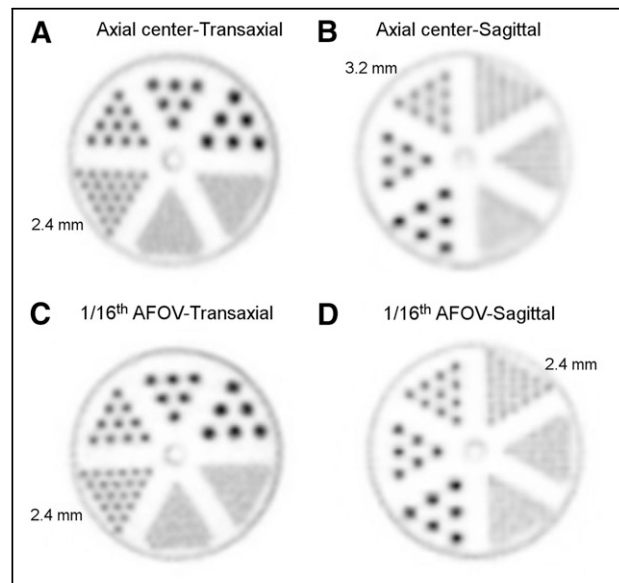

FIGURE 5. Reconstructed image slices of mini-Derenzo phantom imaged at axial center (A and B) and $\frac{1}{16}$ AFOV (C and D) and with 2 orientations: transaxial (A and C) and sagittal (B and D). Image slice thickness is 1.172 mm.

TABLE 1
Spatial Resolution of ^{18}F Point Sources Measured with Fourier-Rebinned Filtered Backprojection Reconstruction

Location	Position	Full width at half maximum (mm)		
		Tangential	Radial	Axial
Center AFOV	1 cm	3.0	3.0	2.8
	10 cm	3.1	3.4	3.2
	20 cm	4.0	4.7	3.2
$^{1}/_{8}$ AFOV	1 cm	2.9	3.0	2.9
	10 cm	3.2	3.6	3.1
	20 cm	4.4	4.6	3.3

resolved at both positions. In the sagittal orientation, the 2.4-mm rods were mostly resolved when scanned with 1 PET unit ($^{1}/_{16}$ AFOV), whereas the minimum rod resolvability was 3.2 mm at the axial center. This result agrees with previous findings, which demonstrated an approximately 0.5-mm degradation in axial spatial resolution with a similar acceptance angle comparison (*35*).

Image Quality and Accuracy of Corrections

The results for contrast recovery and background variability with the NEMA IQ phantom at the axial center of the field of view are shown in Figure 6. The choice of reconstruction parameters has a large impact on CRC, particularly for the smallest sphere (10 mm); using our clinical image reconstruction protocol with no PSF modeling, the CRC was 49.8%, whereas with our high-resolution brain reconstruction parameters (1.17-mm voxels, 10 iterations) with PSF modeling it increased to 69.2%. The background variability was very low in all reconstruction modes and ROI sizes, ranging from 1.2% to 4.3%. The relative count error in the lung insert was 1.36% and 2.88% using the clinical image reconstruction protocol with and without PSF modeling, respectively, whereas it was 0.00% with the high-resolution brain reconstruction protocol.

Contrast recovery and background variability as a function of scan time and activity are shown in Figure 7. Contrast recovery was stable when reducing the scan duration or activity to 30% of the standard values for all sphere sizes. Furthermore, the contrast recovery of the 4 larger spheres was not affected when reducing the scan time or activity to 10%. Similarly, background variability stayed below 7%, even for the 10-mm sphere size, when scan duration or activity was decreased to 10% of the original value. Example images of the central slice of the 30-min scan of the IQ phantom at 0-, 3-, 6-, 9-, and 12-h delayed time points (Fig. 7E) gives a qualitative assessment of the image quality at different activity levels. Additional images with reduced scan times and activities are shown in Supplemental Figure 2.

The evaluation of the uEXPLORER IQ throughout the AFOV is depicted in Table 2, which provides the CRC and background variability from 5 scans at 5 axial positions for 2 representative spheres (37 and 22 mm). The images of the 5 scans are shown in Supplemental Figure 3. The results show that CRC was not significantly affected throughout the AFOV, whereas there was a small increase in background variability at the edges of the field of view, where the scanner has lower sensitivity (70% compared with peak sensitivity at the center).
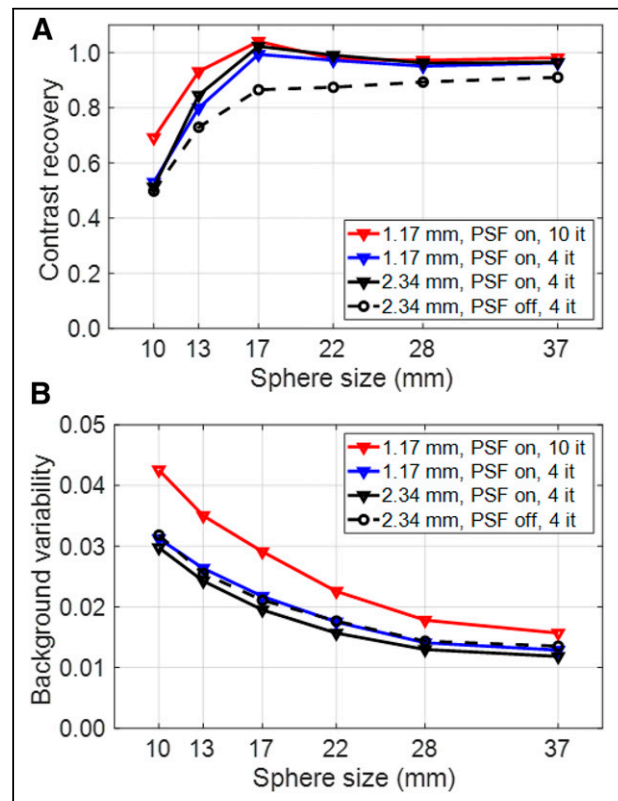

FIGURE 6. Contrast recovery (A) and background variability (B) measured with standard NEMA IQ phantom evaluation placed at center of AFOV and scanned for 30 min.

Finally, the effect of sphere-to-background ratio on contrast recovery of all spheres is shown in Supplemental Figure 4; the CRC of the smallest sphere was improved to 93.9%, with a sphere-to-background ratio of 9.0:1.

Human Imaging

Human imaging results illustrating the spatial resolution, sensitivity, and overall image quality of the uEXPLORER are provided in Figure 8. The acquisition parameters of these studies are summarized in Table 3, along with the singles, prompts, and randoms count-rates and estimated dead-time fraction. Estimated dead time for human studies was calculated using the dead-time fractions obtained with the 175-cm phantom experiment at the corresponding effective activity concentrations for each human PET exam (4.1 kBq/mL for the ^{18}F-fluciclovine subject and 1.4 kBq/mL for the ^{18}F-FDG subject).

The transaxial images shown in Figure 8A demonstrate that the excellent spatial resolution of the uEXPLORER enabled clear tracer localization within a pulmonary nodule measured to be 2.5 mm in diameter on the CT scan.

The high sensitivity and image quality attributes of the uEXPLORER could be displayed using reconstructions of shortened scan durations extracted from a representative 20-min ^{18}F-FDG PET scan of a lung cancer patient. This clinical oncology total-body PET protocol was achieved with half the standard injected activity (~185 MBq) of conventional whole-body PET at our institution and was acquired 30 min later (90 min), yet a 5-min acquisition still demonstrated excellent image quality. Although
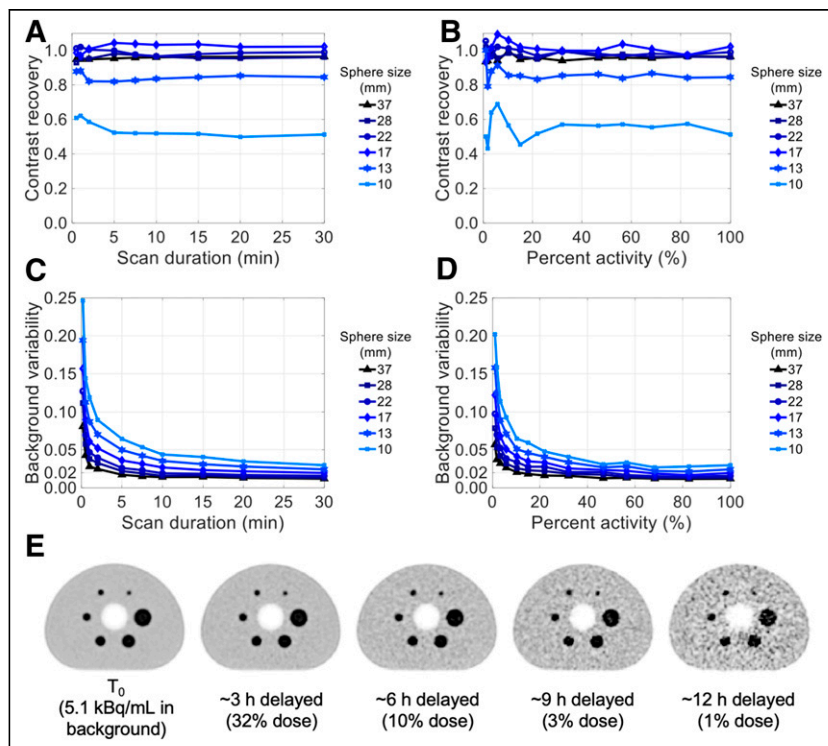
FIGURE 7. Contrast recovery (A and B) and background variability (C and D) as function of scan duration (A and C) and activity (B and D). Percentage activity is relative to initial activity in phantom at starting time of scans. (E) Transaxial image slices of 30-min scan at several imaging timepoints reconstructed using clinical protocol. All images are decay-corrected and use same color scale: 0–20 kBq/mL.

image noise noticeably increased with shorter acquisition times, all lesions, including a small (~1 cm) ^{18}F-FDG–avid adrenal lesion, could be visualized in the 2.5-min acquisition.

In Supplemental Figure 5, the effect of scan duration on coefficient of variation is shown for a homogeneous 37-mm-dimeter spheric ROI placed in the patient liver and likewise in the background of the NEMA IQ phantom acquired at a similar activity concentration to that of the patient liver and with matched reconstruction parameters. The trend in coefficient of variation versus the duration of this human scan closely mirrored the trends in coefficient of variation measured in the NEMA IQ phantom. The approximately 25% positive bias in coefficient of variation in the

liver, compared with the phantom, may be a result of patient motion (respiration), anatomic inhomogeneities, or differences in the accuracy of data corrections (e.g., scatter and attenuation).

DISCUSSION

The dominant physical performance attribute of the uEXPLORER total-body PET system is its high sensitivity, which cannot be fully reflected with the NEMA NU 2-2018 standard. Therefore, an alternative measurement with an approximately average human-sized (27) 170-cm-long line source was required. If we extrapolate the published 70-cm NEMA NU 2-2018 sensitivities for state-of-the-art PET systems with a conventional AFOV of less than 25 cm (15–22) to what would be obtained with the total-body 170-cm-long line source (i.e., multiply the published NEMA NU 2 values by 70 cm/ 170 cm, which is a valid mathematic representation of the reduced activity per unit length in the 170-cm-long line source measurement for scanners with an AFOV of <70 cm), the 147 kcps/MBq total-body sensitivity of the uEXPLORER represents a 15- to 68-fold gain compared with current state-of-the-art conventional systems as predicted by the prior simulation work (1,2). Although a wider acceptance angle than the fixed ±4 maximum unit difference would provide higher line source sensitivity, in practice for human imaging the optimal acceptance angle depends on several effects, including the patient size and activity distribution and the overall concentration, and is a subject of future investigations. The high sensitivity provided by the 194-cm AFOV is further evidenced by the excellent image quality obtained with low-activity imaging, short-duration acquisitions, or considerably delayed scans (Figs. 7 and 8).

The total sensitivity was higher for the 70-cm line source than for the 170-cm line source, as expected from the reduced geometric efficiency toward the ends of the scanner; however, the peak NECR with the 175-cm-long scatter phantom was higher than that for the 70-cm-long scatter phantom. This difference can be explained by differences in attenuation and dead-time losses,

TABLE 2
Contrast Recovery and Background Variability at 5 Locations Along AFOV

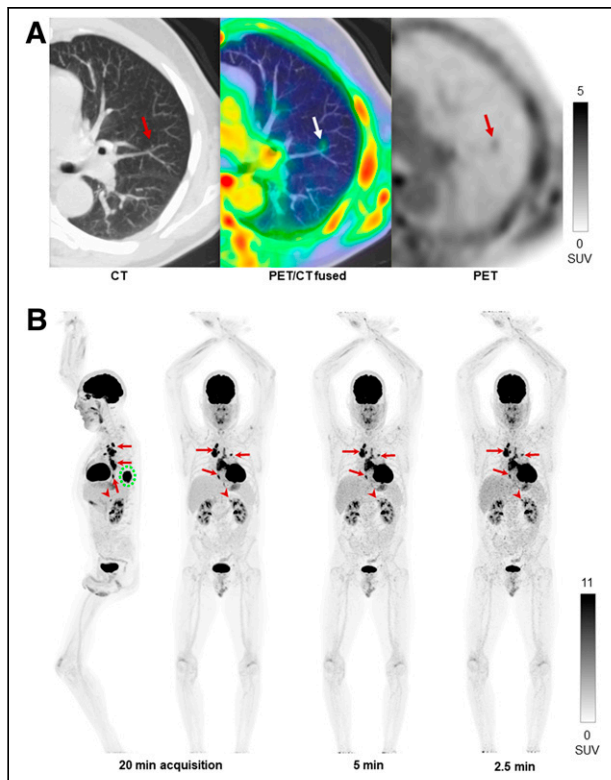| Axial position	Background activity (kBq/mL)	Scan duration	37-mm sphere		22-mm sphere	
			CRC	Background variability	CRC	Background variability
−63 cm (1/20 AFOV)	3.3	10.5 min	96.8%	1.4%	94.7%	2.8%
−39 cm (3/10 AFOV)	3.6	9.6 min	96.7%	1.7%	96.8%	2.4%
0 cm (center)	4.5	7.6 min	95.8%	1.6%	98.9%	1.9%
+39 cm (7/10 AFOV)	2.9	11.7 min	94.7%	1.6%	96.7%	2.4%
+63 cm (9/10 AFOV)	2.7	13.0 min	91.5%	1.8%	90.4%	2.5%

FIGURE 8. Human imaging examples of performance of uEXPLORER total-body PET scanner. (A) Axial slice from ^{18}F-fluciclovine PET image (right), with corresponding fused image (middle) and CT image (left), of 68-y-old patient with castration-resistant metastatic prostate cancer, demonstrating clear visualization of ^{18}F-flucicovine accumulation within 2.5-mm-diameter pulmonary nodule. (B) Maximum-intensity projection of representative clinical oncology ^{18}F-FDG PET scan reconstructed with 20-, 5-, and 2.5-min durations, of 59-y-old patient with lung cancer. Images show primary tumor in left lower lobe of lung (dashed circle), with multiple variable-sized (0.8–6 cm) hilar, mediastinal, and lower esophageal nodal metastases (arrows) and ~1-cm ^{18}F-FDG–avid left adrenal nodule (arrowhead), which is visualized for all scan durations.

which depend on the phantom length. First, by examining the slope of the ideal trues count rate versus total activity for both the 70-cm and the 175-cm scatter phantoms (Supplemental Fig. 1), we found that very similar values were obtained for both phantom lengths. Although the sensitivity results suggest higher trues

sensitivity for phantoms with a shorter line source, the impact of attenuation was greater in the 70-cm phantom at the center of the AFOV than in the extended 175-cm phantom. This greater impact is due to the larger relative abundance of oblique LORs with the 70-cm phantom at the axial center versus the 175-cm phantom, which extends close to the ends of the scanner, where the acceptance angle is reduced.

Second, distributing a given amount of activity over a wider extent of the field of view with the longer phantom leads to lower average singles rates for the LORs that intersect the phantom, compared with the axially concentrated activity distribution in the 70-cm scatter phantom. The result is a reduced dead-time fraction with the 175-cm phantom versus the 70-cm phantom at matched levels of total activity. Although the ratio of trues to dead-time loss at the respective peak NECR activities was 34% for both phantom lengths, the longer phantom reached peak NECR at a higher absolute activity and therefore provides a higher absolute trues rate and NECR.

The remaining factor that impacts the NECR at high activities is the randoms. The use of a wide acceptance angle in the 194-cm-long scanner necessitates the use of a relatively wide coincidence timing window for oblique LORs. So, whereas the absolute dead-time losses at each activity are lower with the 175-cm phantom, which therefore provides better trues linearity than the 70-cm phantom, as shown in Figure 3 and Supplemental Figure 1, this lowering of the dead-time losses is eventually overwhelmed by the large increase in randoms at high activities and becomes the limiting factor for peak NECR. The small activity-dependent increase in scatter fraction observed in both scatter phantom measurements may be a result of pulse pile-up, which causes crystal misidentification in the flood maps, a common effect in PET systems that use light-sharing block detectors. However, a detailed investigation of the relationships between count rates, NECR, and image quality metrics is needed in future work.

In Supplemental Figure 1, the count rates for both phantoms are plotted relative to absolute activity rather than activity concentration, and the described effects can be clearly seen: whereas the slope of the ideal trues count rates are nearly identical for both the 70-cm and the 175-cm scatter phantoms, indicating equivalent geometric trues sensitivity for both phantoms, the dead-time losses and dead-time fraction are universally lower in the 175-cm-long scatter phantom than in the 70-cm-long scatter phantom and results in an increased peak NECR with the longer phantom, compared with the NEMA NU 2-2018 measurement. Measuring the NECR of a total-body PET scanner using a 70-cm phantom does not translate to a very useful metric for clinical total-body

TABLE 3
Parameters Associated with Images Displayed in Figure 8

Figure	Image	Injected dose	Subject weight	Time point	Scan duration	Singles/prompts/randoms	Dead-time fraction
8A	Transaxial slices	320 MBq ^{18}F-fluciclovine	76 kg	4 min after injection	10-min	101/24.7/18.3 Mcps	14.4%
8B	Maximum-intensity projection	188 MBq ^{18}F-FDG	93 kg	90 min after injection	20, 5, and 2.5 min	19.6/4.4/2.2 Mcps	1.2%

Count rates were extracted from list-mode tags; dead-time fractions were estimated according to dead-time fractions at equivalent activity concentration with 175-cm scatter phantom.

PET human imaging; however, the peak NECR for a human-sized 175-cm phantom should directly translate to an estimate for the peak NECR during total-body human imaging with clinically appropriate activity levels. This observation further demonstrates the need for a new set of measurements to characterize total-body PET scanners.

The measured NECR characteristics have several implications for clinical use. First, the high peak NECR for both the 70-cm NEMA NU 2-2018 and the extended 175-cm phantom measurements supports the use of total-body PET for improving image quality (reduced statistical noise), the use of short frames (e.g., ≤1 s) for dynamic imaging, and the use of a reduced scan duration (<1 min). Although the NECR peaks at an activity concentration above the concentrations encountered in any uEXPLORER study to date, some applications that involve highly concentrated and large total activities (e.g., ^{82}Rb and ^{15}O-H$_2$O) may be dose-limited; however, a detailed investigation is needed in this regard.

The extended phantom measurements presented here are suitable for adoption in the characterization of other long-AFOV PET systems. Although a 70-cm-long phantom may well approximate the count rates encountered in conventional PET exams, for which a large fraction of the imaging subject and activity is outside the scanner field of view at any one time, extended-AFOV and single-bed-position imaging requires the use of phantoms with lengths that better represent the extent of the activity biodistribution in clinical PET studies. Therefore, we expect that our presented phantom measurements with 170- to 175-cm phantoms that were modeled from the NEMA NU 2 standard will serve as a reasonable starting point for future long-AFOV scanner characterizations.

PET data correction methods currently used for the uEXPLORER have been extended from conventional approaches. However, quantification in such a large system with the inclusion of highly oblique LORs poses many new challenges to the models and assumptions encountered in conventional PET data corrections. With the emphasis of this study being on the physics characterization of the first total-body PET scanner, a complementary investigation of quantitation in total-body PET will soon be forthcoming.

The discrepancy between the global TOF resolution (505 ps) and the average TOF resolution calculated from individual LOR TOF histograms (412 ps) likely indicates an incomplete TOF calibration. With more than 500,000 crystals forming almost 100 billion LORs, accurately calibrating the TOF offsets in the uEXPLORER is challenging using the existing methods that were developed for much shorter PET systems. Work in this area is ongoing.

The use of LYSO crystals with a small cross-section provides spatial resolution of about 3 mm in full width at half maximum (Table 1), the smallest NEMA NU 2 resolution for any whole-body PET/CT system to date. Combined with its high sensitivity, the uEXPLORER is able to produce reconstructed images with small voxel sizes (e.g., 1.17-mm isotropic voxels) while maintaining lower background variability than in conventional PET systems, which universally use larger voxel sizes and postreconstruction smoothing (Fig. 6). The increase in contrast recovery with small voxels coupled with low background variability is likely of high interest for clinical PET imaging, such as in detecting and quantifying uptake in smaller lesions, although clinical validation is needed.

When the image quality figures-of-merit obtained with the NEMA IQ phantom are compared with conventional whole-body PET systems, the uEXPLORER offers high CRC, particularly for the small sphere sizes (10 and 13 mm), because of the fine spatial resolution provided by a small detector pixel size. Although no modifications were made to the spheres embedded in the NEMA IQ phantom for these measurements, recent developments in PET sensitivity and spatial resolution, including—most notably in this work—the detection of lung lesions smaller than 5 mm with ^{18}F-fluciclovine, suggest precedence to revisit the standardized methods and phantom sphere sizes used to evaluate contrast recovery in clinical PET systems. Future evaluation studies with the total-body uEXPLORER system will include a detailed investigation of the detection limits in high-sensitivity and high-resolution total-body PET. As expected from the high sensitivity of the scanner, background variability was approximately 1.8- to 3.0-fold lower than that in other current state-of-the-art conventional PET systems (15–17,19–22). Lastly, the similarity between image quality metrics obtained with reduced scan durations and those obtained with reduced activity concentrations (delayed scan) suggests that the increased LYSO background radiation from the large volume of ^{176}Lu in the uEXPLORER, compared with conventional PET systems, has minimal impact on image quality for activity concentrations of as low as approximately 0.1 kBq/mL.

A critical parameter in any PET system, but especially so in long-AFOV PET, is the uniformity of image quality throughout the AFOV. In long-AFOV PET, however, this parameter cannot be entirely characterized in a single scan with the available short-length IQ phantoms. To address this limitation, we imaged the NEMA IQ phantom at 5 different axial positions along the AFOV. Excellent uniformity in CRC and background variability was measured as the phantom moved from the center of the AFOV to a ±63-cm offset from the center. With the 2 tested sphere sizes, the SD of CRC and background variability at 5 axial positions were below 3% and 0.3%, respectively. Importantly, consistent background variability measured within the central 125-cm span of the AFOV illustrates the result of the plateau in peak sensitivity within the central approximately 120 cm of the AFOV as shown in the total-body axial sensitivity profile (Fig. 2B), and which is provided uniquely by the 57.0° acceptance angle and the 194-cm total AFOV. Overall, the image quality evaluation suggests that the uEXPLORER can provide excellent imaging capabilities for routine clinical studies and in a variety of imaging regimes, spanning ultra-low-dose imaging with ^{18}F delayed for up to 12 h and short dynamic frames.

CONCLUSION

This study was the first performance evaluation of the 194-cm-long uEXPLORER total-body PET/CT system using the standard NEMA NU 2-2018 measurements, as well as newly devised measurements to fully characterize the long-AFOV PET scanner, which is not well served by the current NEMA NU 2 standards. The total-body system exhibits high sensitivity (174 kcps/MBq with NEMA NU 2-2018, 147 kcps/MBq with a 170-cm human-sized line source) and similarly high count-rate performance that follows from the high geometric sensitivity of the long-AFOV system, with a peak NECR of 1,524 kcps with NEMA NU 2-2018 and 1,855 kcps for the extended 175-cm total-body imaging phantom. Count-rate results further indicate that NECR becomes limited by dead-time losses and a high randoms fraction beyond approximately 370 MBq. The small LYSO crystal size coupled with high sensitivity allows for spatial resolution of about 3.0 mm, as demonstrated in both phantom scans and clinical imaging. Together, these system attributes enable excellent image quality and low statistical noise in both phantom evaluations and clinical studies. This total-body PET system represents a step-change in performance that opens up a

wide range of new opportunities in research to study total-body tracer kinetics in systemic and multiorgan disease and in clinical practice, where protocols can be tailored to emphasize exceptional image quality, short scan duration, low radiation dose, or delayed imaging as dictated by the clinical question at hand.

DISCLOSURE

ACKNOWLEDGMENTS

KEY POINTS

QUESTION: What is the performance of the first-ever total-body PET scanner using standard NEMA NU 2-2018 tests, and how can these tests be extended to provide a more informative evaluation of PET scanners with an AFOV that exceeds what was envisioned when the NEMA tests were devised?

PERTINENT FINDINGS: The EXPLORER total-body PET scanner exhibits the highest sensitivity and count-rate performance of any available PET/CT scanner, which, coupled with its spatial resolution of about 3 mm, produces a step change in image quality achievable with PET.

IMPLICATIONS FOR PATIENT CARE: This ultra-high-sensitivity scanner is already being used in routine clinical service to decrease patient dose while dramatically improving image quality.

REFERENCES

1. Poon, JK, Dahlbom, ML, Moses, WW. Optimal whole-body PET scanner configurations for different volumes of LSO scintillator: a simulation study. *Phys Med Biol.* 2012;57:4077–4094.
2. Poon, JK. *The Performance Limits of Long Axial Field of View PET Scanners.* Thesis. University of California, Davis; 2013.
3. Badawi, RD, Lewellen, TK, Harrison, RL, Kohlmyer, SG, Vannoy, SD. The effect of camera geometry on singles flux, scatter fraction and trues and randoms sensitivity for cylindrical 3D PET: a simulation study. *IEEE Trans Nucl Sci.* 2000;47:1228–1232.
4. Surti, S, Karp, JS. Impact of detector design on imaging performance of a long axial field-of-view, whole-body PET scanner. *Phys Med Biol.* 2015;60:5343–5358.
5. Surti, S, Werner, ME, Karp, JS. Study of PET scanner designs using clinical metrics to optimize the scanner axial FOV and crystal thickness. *Phys Med Biol.* 2013;58:3995–4012.
6. MacDonald, LR, Harrison, RL, Alessio, AM, Hunter, WCJ, Lewellen, TK, Kinahan, PE. Effective count rates for PET scanners with reduced and extended axial field of view. *Phys Med Biol.* 2011;56:3629–3643.
7. Couceiro, M, Ferreira, NC, Fonte, P. Sensitivity assessment of wide axial field of view PET systems via Monte Carlo simulations of NEMA-like measurements. *Nucl Instrum Meth A.* 2007;580:485–488.
8. Cherry, SR, Badawi, RD, Karp, JS, Moses, WW, Price, P, Jones, T. Total-body imaging: transforming the role of positron emission tomography. *Sci Transl Med.* 2017;9:eaaf6169.
9. Cherry, SR, Jones, T, Karp, JS, Qi, J, Moses, WW, Badawi, RD. Total-body PET: maximizing sensitivity to create new opportunities for clinical research and patient care. *J Nucl Med.* 2018;59:3–12.
10. Our team. EXPLORER Total-Body PET Scanner website. https://explorer.ucdavis.edu/our-team. Accessed January 26, 2021.
11. Karp, JS, Viswanath, V, Geagan, MJ. PennPET Explorer: design and preliminary performance of a whole-body imager. *J Nucl Med.* 2020;61:136–143.
12. Pantel, AR, Viswanath, V, Daube-Withersponn, M. PennPET Explorer: human imaging on a whole-body imager. *J Nucl Med.* 2020;61:144–151.
13. Watanabe, M, Shimizu, K, Omura, T. A high-throughput whole-body PET scanner using flat panel PS-PMTs. *IEEE Trans Nucl Sci.* 2004;51:796–800.
14. Conti, M, Bendriem, B, Casey, M. Performance of a high sensitivity PET scanner based on LSO panel detectors. *IEEE Trans Nucl Sci.* 2006;53:1136–1142.
15. Hsu, DFC, Ilan, E, Peterson, WT, Uribe, J, Lubberink, M, Levin, CS. Studies of a next-generation silicon-photomultiplier-based time-of-flight PET/CT system. *J Nucl Med.* 2017;58:1511–1518.
16. van Sluis, J, de Jong, J, Schaar, J. Performance characteristics of the digital Biograph Vision PET/CT system. *J Nucl Med.* 2019;60:1031–1036.
17. Rausch, I, Ruiz, A, Valverde-Pascual, I, Cal-Gonzalez, J, Beyer, T, Carrio, I. Performance evaluation of the Vereos PET/CT system according to the NEMA NU2-2012 standard. *J Nucl Med.* 2019;60:561–567.
18. Jakoby, BW, Bercier, Y, Conti, M, Casey, ME, Bendriem, B, Townsend, DW. Physical and clinical performance of the mCT time-of-flight PET/CT scanner. *Phys Med Biol.* 2011;56:2375–2389.
19. Bettinardi, V, Presotto, L, Rapisarda, E, Picchio, M, Gianolli, L, Gilardi, MC. Physical performance of the new hybrid PET/CT Discovery-690. *Med Phys.* 2011;38:5394–5411.
20. Kolthammer, JA, Su, KH, Grover, A, Narayanan, M, Jordan, DW, Muzic, RF. Performance evaluation of the Ingenuity TF PET/CT scanner with a focus on high count-rate conditions. *Phys Med Biol.* 2014;59:3843–3859.
21. Delso, G, Fürst, S, Jakoby, B. Performance measurements of the Siemens mMR integrated whole-body PET/MR scanner. *J Nucl Med.* 2011;52:1914–1922.
22. Grant, AM, Deller, TW, Khalighi, MM, Maramraji, SH, Delso, G, Levin, CS. NEMA NU 2-2012 performance studies for the SiPM-based ToF-PET component of the GE SIGNA PET/MR system. *Med Phys.* 2016;43:2334–2343.
23. Conti, M, Bharkhada, D, Cabello, J. Design considerations for an ultra-long axial FOV PET/CT scanner [abstract]. *J Nucl Med.* 2020;61(suppl 1):314.
24. Niedzwiecki, S, Bialas, P, Curceanu, C. J-PET: a new technology for the whole-body PET imaging. *Acta Phys Pol B Proc Suppl.* 2017;48:1567.
25. Badawi, RD, Shi, H, Hu, P. First in human imaging studies with the EXPLORER total-body PET scanner. *J Nucl Med.* 2019;60:299–303.
26. Zhang, X, Cherry, SR, Zhaoheng, X, Hongcheng, S, Badawi, RD, Qi, J. Subsecond total-body imaging using ultrasensitive positron emission tomography. *Proc Natl Acad Sci USA.* 2020;117:2265–2267.
27. *NEMA Standards Publication NU 2-2018: Performance Measurements of Positron Emission Tomographs (PET).* National Electrical Manufacturers Association; 2018.
28. NCD Risk Factor Collaboration (NCD-RisC). A century of trends in adult human height. *eLife.* 2016;5:13410.
29. Tang, S, Liu, Y, Wang, J, Zhao, Y, Fan, X, Dong, Y. Dead time correction method for long axial field-of-view, whole-body PET scanner [abstract]. *J Nucl Med.* 2019;60(suppl 1):458.
30. Tang, S, Zhao, Y, Wang, J, Liu, Y, Dong, Y. Geometric correction in normalization for long axial field-of-view, whole-body PET scanner. Poster presented at: the 2019 Nuclear Science Symposium (NSS) and Medical Imaging Conference (MIC), and the International Symposium on Room Temperature Semiconductor Detectors (RTSD); October 26 to November 2, 2019; Manchester, U.K.
31. He, L, Deng, Z, Ding, Y, Zhao, Y, Hu, D, Dong, Y. Validation of scatter correction with Monte Carlo simulation for uEXPLORER [abstract]. *J Nucl Med.* 2019;60(suppl 1):45.
32. Zhang, X, Zhou, J, Cherry, SR, Badawi, RD, Qi, J. Quantitative image reconstruction for total-body PET imaging using the 2-meter long EXPLORER scanner. *Phys Med Biol.* 2017;62:2465–2485.
33. Zhao, Y, Deng, Z, Lv, Y, Hu, D, Ding, Y, Dong, Y. Image quality evaluation of analytic reconstruction algorithms for long axial field-of-view PET scanner [abstract]. *J Nucl Med.* 2019;60(suppl 1):240.
34. Defrise, M, Kinahan, PE, Townsend, DW. Exact and approximate rebinning algorithms for 3-D PET data. *IEEE Trans Med Imaging.* 1997;16:145–158.
35. Berg, E, Zhang, X, Bec, J. Development and evaluation of mini-EXPLORER: a long axial field-of-view PET scanner for nonhuman primate imaging. *J Nucl Med.* 2018;59:993–998.